ARTICLE   OPEN

Dual-phase MoS₂/MXene/CNT ternary nanohybrids for efficient electrocatalytic hydrogen evolution

Sichen Wei[1], Yu Fu[1], Maomao Liu[2], Hongyan Yue[3], Sehwan Park[4], Young Hee Lee [4], Huamin Li [2✉] and Fei Yao[1✉]

Two-dimensional (2D) molybdenum disulfide (MoS₂) has been recognized as a potential substitution of platinum (Pt) for electrochemical hydrogen evolution reaction (HER). However, the broad adoption of MoS₂ is hindered by its limited number of active sites and low inherent electrical conductivity. In this work, we employed a one-step solvothermal synthesis technique to construct a ternary hybrid structure consisting of dual-phase MoS₂, titanium carbide (Ti₃C₂) MXene, and carbon nanotubes (CNTs), and demonstrated synergistic effects for active site exposure, surface area enlargement, and electrical conductivity improvement of the catalyst. The dual-phase MoS₂ (DP-MoS₂) is directly formed on the MXene with CNTs acting as crosslinks between 2D islands. The existence of edge-enriched metallic phase MoS₂, the conductive backbone of MXene along with the crosslink function of CNTs clearly improves the overall HER performance of the ternary nanocomposite. Moreover, the integration of MoS₂ with MXene not only increases the interlayer distance of the 2D layers but also partially suppresses the MXene oxidation and the 2D layer restacking, leading to good catalytic stability. As a result, an overpotential of 169 mV and a low Tafel slope of 51 mV/dec was successfully achieved. This work paves a way for 2D-based electrocatalyst engineering and sheds light on the development of the next-generation noble metal-free HER electrocatalysts.

INTRODUCTION

Hydrogen shows great potential in reducing greenhouse gas emissions and improving energy efficiency due to its environmentally friendly nature and inherent high gravimetric energy density[1–3]. Hydrogen gas can be generated via electrochemical water splitting based on the hydrogen evolution reaction (HER, $2H^+ + 2e^- \rightarrow H_2$)[4,5]. HER is a multistep reaction that starts with a Volmer step ($H^+ + e^- + * \rightarrow H_{ads}$). The intermediate H_{ads} is removed from the catalyst surface either by Tafel reaction ($H_{ads} + H_{ads} \rightarrow H_2 + 2*$) or by Heyrovsky reaction ($H^+ + H_{ads} + e^- \rightarrow H_2 + *$)[6,7]. The reaction kinetics is greatly affected by the number of available active sites (represented as * in the equation), the way H_{ads} interacts with the catalyst surface (i.e., hydrogen adsorption energy ΔG_{ads}), and electron transfer rate. It is well known that Pt-group metals (PGM) are excellent catalysts for HER, but their practical applications are limited by the high cost and scarcity[1,7,8]. Therefore, the development of active HER catalysts made from low-cost materials is the key step in the utilization of hydrogen energy.

Recently, non-precious elements have been widely employed to construct HER catalysts which can be classified into two major groups including transition metals (such as Mo, W, and Co, *etc.*) and nonmetals (such as S, Se, and C, etc.). To date, efficient PGM-free HER electrocatalysts synthesized based on the above-mentioned non-precious elements have demonstrated outstanding HER catalytic activities because of their unique physical and chemical properties[6,9]. For instance, ideal H adsorption energy, high metallicity, and PGM-like electronic configuration along with chemical environmental compatibility have been identified as origins of superior HER activity for metal sulfide/selenides/carbides[6,10,11]. Among them, two-dimensional (2D) molybdenum

disulfide (MoS₂) is regarded as a promising alternative to Pt due to its large surface area, near-zero ΔG_{ads}, and numerous structure engineering possibilities[3,12]. The material properties of MoS₂ are determined by its polymorph types, namely hexagonal 2H or trigonal 1T phases. The intrinsically low electrical conductivity arising from the semiconducting nature of the 2H phase hinders the development of MoS₂-based electrocatalysts. Tremendous efforts have been devoted to improving the conductivity of 2H-MoS₂ via inducing phase transition from semiconducting 2H phase to metallic 1T phase through ion intercalation, doping engineering, and strain application, etc.[13–16]. Among them, solution-phase-based ion intercalation achieved during MoS₂ hydrothermal/solvothermal synthesis has been considered as one of the most effective approaches for phase engineering. Compared to multistep electrochemical/chemical intercalations where post-synthetic treatments are normally required, such a process enables ion intercalation along with MoS₂ synthesis in a single step one-pot reaction and produces highly active, defect-rich 1T MoS₂ with high surface area, offering significant advantages such as simplicity, low cost, scalability, operational stability, and environmental friendliness due to the use of benign precursors/solvents[17]. Compared with a hydrothermal synthesis which is widely used for producing various MoS₂ structures including nanosheets, nanodots, and nanoflowers with different 1T phase ratios[18], solvothermal synthesis involving the use of bisolvent has been rarely explored. The use of bisolvent will increase the solubility of MoS₂ precursors, trigger deep 2H to 1T phase transition and prevent from undesired oxidation reaction which is of particular importance for sensitive materials, such as MXene.

[1]Department of Materials Design and Innovation, University at Buffalo, the State University of New York, Buffalo, NY 14260, USA. [2]Department of Electrical Engineering, University at Buffalo, the State University of New York, Buffalo, NY 14260, USA. [3]School of Materials Science and Engineering, Harbin University of Science and Technology, Harbin 150040, China. [4]Center for Integrated Nanostructure Physics, Institute for Basic Science, Department of Energy & Department of Physics, Sungkyunkwan University, Suwon, Gyeonggi-do 16419, South Korea. ✉email: huaminli@buffalo.edu; feiyao@buffalo.edu
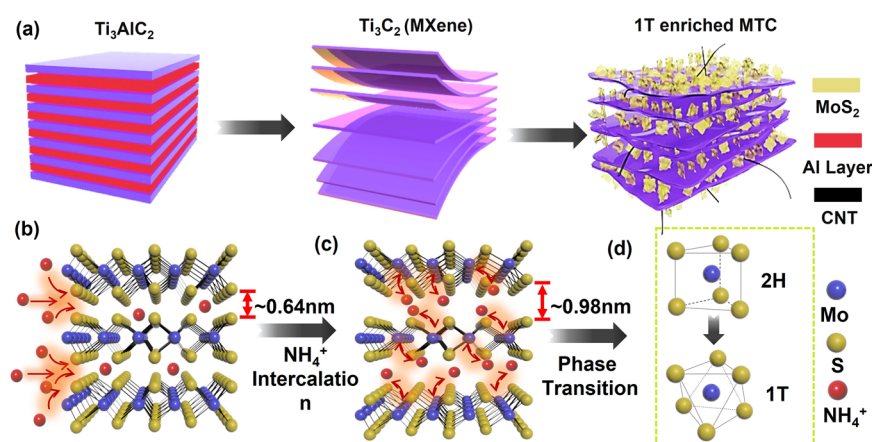
Fig. 1 Schematic illustration of sample preparation. a Schematic illustrations of the preparation of 1 T enriched-MoS$_2$/MXene/CNT composite through one-step solvothermal technique. The mechanism of ammonia ion intercalation induced MoS$_2$ phase transition is shown in **b**–**d**.

MXene (M$_{n+1}$X$_n$T$_x$, where "M" represents early transition metal, "X" is carbon and/or nitrogen, and T$_x$ is surface functional groups in the chemical formula) is a group of materials consisting of transition metal carbides/nitrides/carbonitrides, which are produced by selectively etching of "A" element from MAX phase ("A" is group IIIA and IVA element)[19,20]. It has been widely investigated in supercapacitors and aqueous batteries because of its high conductivity, excellent hydrophilicity, and large interlayer distance[21–24]. Compared with charge-neutral graphene, MXene exhibits a negatively charged surface due to the existence of enriched surface functional groups, including -OH, -O, and -F, etc.[22,25]. These surface functional groups will not only enhance the dispersion of precursors but also promote the MoS$_2$ nucleation in bisolvent, making it a superior substrate for the synthesis of MoS$_2$[26]. Especially, oxygen-containing functional groups have been proved with near-zero ΔG_{ads}, suggesting potentially catalytic activity for the HER[27,28]. Recently, 2H-MoS$_2$ has been integrated with different types of MXene using in-situ sulfidation[29] and microwave-assisted growth methods[26]. The hybrid structures delivered an exceptional catalytic activity and durability for HER. Nevertheless, the above-mentioned strategies normally require multiple engineering processes involving complicated experimental setups that are costly and time-consuming. Hydrothermal methods have also been employed to synthesize 2H-MoS$_2$/MXene composites[30], but the low electrical conductivity of 2H phase MoS$_2$ is still a limiting factor for the overall catalytic performance.

Herein, we design and construct 1 T phase-enriched MoS$_2$ and Ti$_3$C$_2$T$_x$ MXene composites as HER catalysts using a one-step solvothermal method in a bisolvent media. To further improve the catalyst performance, carbon nanotubes (CNT) are introduced in the hybrid structure as crosslinks. The ternary composite not only improves the overall electrical conductivity but also prevents the undesired oxidation and restacking of 2D materials simultaneously. Moreover, we notice that dual-phase MoS$_2$ (DP-MoS$_2$) nanoflakes are vertically integrated with MXene with the exposure of numerous edge sites which are catalytically active for the HER. As a result, an improved HER activity is achieved compared to pure 2H MoS$_2$ and other binary counterparts. The ternary composite exhibits an overpotential of 169 mV which is achieved at a current density of 10 mA/cm^2 and a low Tafel slope of 51 mV/dec with good stability.

RESULTS

Preparation of the dual-phase MTC

The dual-phase MoS$_2$/Ti$_3$C$_2$ MXene/CNT (DP-MTC) samples were prepared by a one-step bisolvent solvothermal synthesis technique and the schematic illustration of the preparation procedure can be found in Fig. 1a. Briefly, few-layered MXene flakes were prepared by the in situ HF etching method[31]. The mixture of MXene and CNT powders were then added into DI water/DMF bisolvent along with ammonium molybdate and thiourea which served as Mo and S sources, respectively. The use of bisolvent is beneficial for promoting MoS$_2$ nucleation by increasing the solubility of MoS$_2$ precursors and improving the conductivity via triggering the 2H to 1 T phase transition through ion intercalation[32–34]. In addition, compared with the pure DI-based hydrothermal method, the adoption of bisolvent will preserve the high conductivity of the MXene matrix by improving the stability of MXene via reducing the undesired oxidation reaction. As shown in Supplementary Figs. 1 and 2, a large amount of TiO$_2$ nanoparticles were found on the surface of the 2H-MoS$_2$/Ti$_3$C$_2$ composite synthesized in DI water along with high oxygen content, which is often observed in the previous reports[35,36]. By contrast, the bisolvent-produced DP- MoS$_2$/ Ti$_3$C$_2$ (Supplementary Fig. 3) showed fewer TiO$_2$ particles and the oxygen content is much lower, demonstrating successfully suppressed oxidation of MXene.

Morphology, phase and structure characterization

To confirm the structure and composition of the products, a series of characterizations were conducted. The SEM images of the as-synthesized materials are shown in Fig. 2. The morphologies of the dual-phase MoS$_2$ (DP-MoS$_2$) nanosheets and MXene layers are shown in Fig. 2a, b, respectively. Compared to the pure DP-MoS$_2$ flakes which exhibit a well-defined nanoflower-like structure with the tendency to form aggregated bundles, DP-MoS$_2$ flakes tend to grow in the interlayers as well as the surface of Ti$_3$C$_2$ MXene, as shown in Fig. 2c. Such a sandwiched binary DP-MoS$_2$/Ti$_3$C$_2$ structure will not only prevent the 2D layers from restacking but also protect the environmentally sensitive MXene from oxidation. The morphology of the ternary DP-MTC100 can be found in Fig. 2d, where the three components are clearly observed. The TEM image of DP-MTC100 (see Fig. 2e, more images can be found in Supplementary Fig. 4a) displays a ternary composite consisting of 1D/2D hybrid structures. Although the density of CNTs is low, they served as a crosslink between the 2D islands and led to the formation of a well-connected conductive network, promoting electron transfer efficiency within the whole system. The EDS elemental mapping can be found in the bottom panel of Fig. 2 (Fig. 2h–l) where the uniform distribution of Mo, S, Ti, and C elements are revealed. The interlayer distance of DP-MoS$_2$ in the as-synthesized ternary composite was extracted from the HRTEM
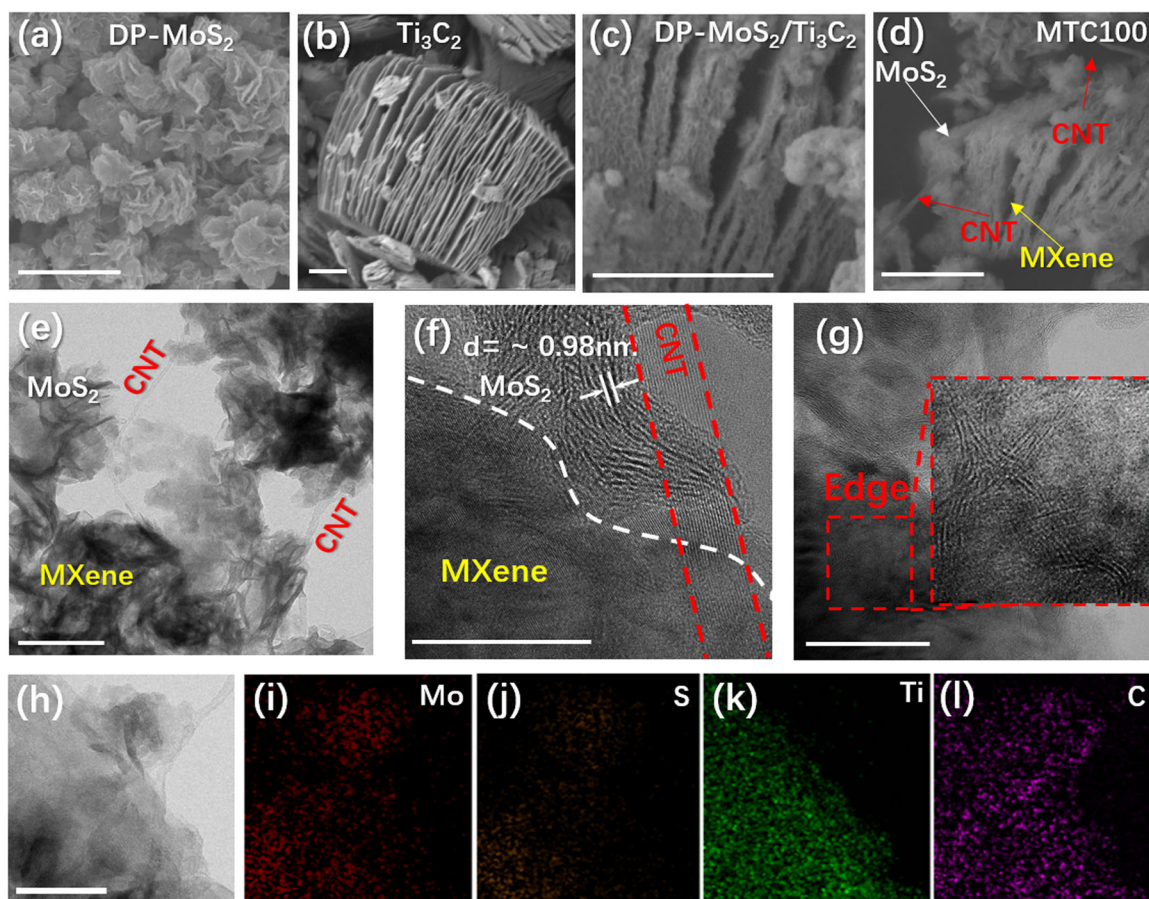
Fig. 2 Morphology characterizations of the ternary structures. a–d are the SEM images of pure 1 T enriched-MoS_2, Ti_3C_2 MXene, MoS_2/Ti_3C_2, and MTC100, respectively. The scale bars are 200 nm, 1 μm, 200 nm, and 200 nm, respectively. **e, f** are the TEM image and HRTEM image of MTC composite, respectively. The scale bars are 200 nm and 20 nm, respectively. The corresponding EDS elemental mapping is shown in **h–l**. The scale bar for panel (**h**) is 100 nm. **g** The HRTEM image of MTC100 and the corresponding enlarged area is displayed to show clear MoS_2 edge structures. The scale bar is 50 nm.

image (Fig. 2f) and the value is ~0.98 nm which is clearly larger than the pure 2H-MoS_2 obtained from in situ sulfurization method (~0.64 nm)[33,34,37]. Besides that, the Ti_3C_2 MXene layers also exhibit an expanded interlayer spacing of ~1.53 nm (Supplementary Fig. 4b) compared to the typical reported value of 1 nm[38]. The increased interlayer space can be ascribed to the NH_4^+ ions intercalation and the integrated stacking nature of the 2D layers, which will be discussed in detail later. Moreover, we notice that a large portion of DP-MoS_2 flakes is in favor of exposing edge sites (Fig. 2g) in the DP-MTC100 composite, leading to the involvement of numerous catalytic active sites for the future HER test.

Figure 3a shows the XRD patterns of various as-prepared samples. The diffraction pattern of Ti_3C_2 MXene shows obvious peaks at 9, 18.4, 27.7, and 60.5 degrees, corresponding to (002), (006), (008), and (110) crystal planes[31,39]. The interlayer distance is extracted to be 0.98 nm and is close to the typical reported value of 1 nm[38]. The absence of the Al peak at~38 degree suggests the successful etching of the Al layer from the MAX precursor[31]. Two peaks located at 35.9 and 41.7 degrees come from TiC, which is the impurity in the MAX phase precursors[40,41]. The DP-MoS_2 obtained via bisolvent synthesis exhibits major diffraction peaks at 9, 33.2, and 58.6 degrees, which are corresponding to the (002), (100), and (110) planes, respectively[33,42]. Compared with the 2H-MoS_2 obtained in aqueous solvent (see Supplementary Fig. 5), the (002) peak has downshifted from ~14 degree to 9 degree, suggesting an expanded interlayer spacing. To analyze in detail, the interlayer spacing has been extracted using Bragg's diffraction

equation, and the value is calculated to be 0.98 nm for DP-MoS_2, which is 0.34 nm larger than the reported value of 2H-MoS_2 (0.64 nm)[34]. In our bisolvent synthesis process, both ammonium molybdate and DMF can act as the abundant source of NH_4^+[33]. Interestingly, the 0.34 nm difference is very close to the size of NH_4^+ ion (0.35 nm), indicating the expanded interlayer spacing of DP-MoS_2 could be attributed to the interaction of NH_4^+ ions, as indicated in Fig. 1b, c. A similar peak shift has been observed for DP-MoS_2/CNT composite as well. In the case of the DP-MoS_2/Ti_3C_2 composite, two peaks located at 6.6 and 8.9 degrees can be clearly identified, corresponding to the (002) planes of Ti_3C_2 and MoS_2 with enlarged interlayer distances of 1.5 nm and 0.99 nm, respectively. This result suggests that the interlayer spacing of both MoS_2 and Ti_3C_2 MXene were expanded simultaneously by forming the MoS_2/Ti_3C_2 composite with the assistance of ion intercalation and integrated 2D layer stackings. Similar interlayer distance expansion is observed in DP-MTC100, which corresponds well with previous TEM observations in Fig. 2f and Supplementary Fig. 4b. However, compared with the DP-MoS_2/Ti_3C_2, no further (002) peak shift is observed in DP-MTC100, indicating that the addition of CNT does not impact the interlayer distance of MoS_2 and Ti_3C_2 MXene.

The Raman spectra of selected samples are shown in Fig. 3b. In the pure Ti_3C_2 MXene Raman spectrum, several peaks that appeared at the lower Raman shift region (below 1000 cm^{-1}) can be attributed to the C-Ti vibrations, and the peaks located at 1341 cm^{-1} and 1583 cm^{-1} reflect the carbon-based *D* band and *G*
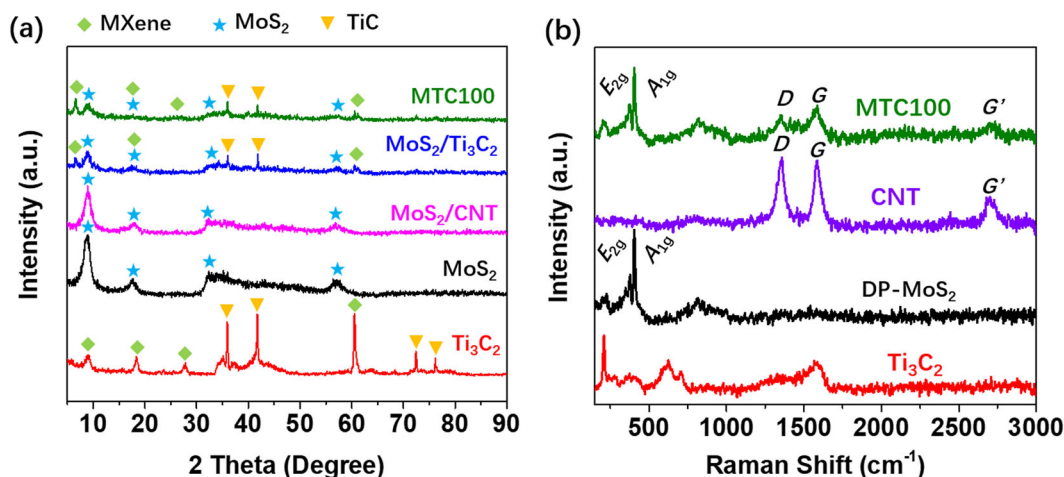
Fig. 3 The structure characterization of the MTC composite. The XRD patterns (**a**) and the Raman spectra (**b**) of various as-synthesized samples.

band vibrations, respectively[43,44]. The as-synthesized DP-MoS$_2$ sample shows the characteristic E_{2g} and A_{1g} vibration peaks at 378 cm^{-1} and 405 cm^{-1}, respectively, corresponding to the 2H phase characteristics[45]. The relative intensity of A_{1g} to E_{2g} peaks provides insightful information related to the MoS$_2$ planes. The out-of-plane A_{1g} vibration mode in MoS$_2$ is preferentially excited for edge-terminated structure due to the polarization dependence[46]. The A_{1g}/E_{2g} ratio is extracted to be as large as 2, indicating an edge-enriched MoS$_2$ structure (see Supplementary Fig. 6)[45]. In addition to the 2H peaks, three 1T-MoS$_2$ related peaks (150, 219, and 336 cm^{-1}) are observed which can be ascribed to J_1, J_2, and J_3 vibration modes, respectively[47]. The coexistence of 1 T and 2H related peaks in the Raman spectrum proves the successful preparation of dual-phase MoS$_2$ using the bisolvent synthesis approach. The broad peak located at 820 cm^{-1} can be attributed to the slightly oxidized MoS$_2$ product[48]. In the case CNTs, the peak located at ~1356 cm^{-1}, 1584 cm^{-1}, and 2695 cm^{-1} can be attributed to the vibration modes of D, G, and G' bands, respectively[49].

The DP-MTC100 sample exhibits both MoS$_2$ related peaks along with CNT-related vibration modes, indicating the successful formation of the ternary composite. It is worth noting that the Ti$_3$C$_2$-related Raman peaks are diminished due to the high surface coverage of MoS$_2$ and the intrinsically weak signal nature of Ti$_3$C$_2$. The unchanged A_{1g}/E_{2g} ratio suggests the edge-enriched MoS$_2$ morphology maintained in the MTC ternary composite, corresponding to the TEM result shown in Fig. 2g. Clear 1T-phase based Raman modes are observed in the MTC hybrid structure (see Supplementary Fig. 6) as well suggesting the coexistence of 2H and 1 T phases in the composite. The formation of the 1 T phase is triggered by the ion intercalation. Specifically, the intercalated NH$_4$$^+$ can stimulate the charge imbalance between Mo^{3+} and Mo^{4+} and cause the S plane sliding and therefore the MoS$_2$ crystal structure distortion along with expanded interlayer spacing, resulting in the phase transformation from 2H to 1 T eventually, as shown in Fig. 1c, d. The existence of the 1 T phase is further proved by the HRTEM image of DP-MTC100, as shown in Supplementary Fig. 4c, where the 1 T phase atomic coordination can be clearly identified.

To investigate the chemical composition of the as-synthesized DP-MTC100, XPS analysis was performed. The complete survey spectrum is shown in Fig. 4a where the characteristic peaks of C, O, Mo, S, and Ti can be clearly observed. To analyze the details for each element, peak deconvolution was carried out. As shown in Fig. 4b, four major peaks located at 284.1 eV, 284.85 eV, 285.85 eV and 287.3 eV for C1s spectra can be ascribed to the C-Mo/C-Ti, C-C,

C-O, and C=O bonds, respectively, which are the typical bonding structures in MXene and CNT[26,50,51]. The peaks at 530.9 eV and 531.6 eV in the O1s spectrum (Fig. 4c) originate from the C-Ti-(OH) and C-Ti-O, respectively, corresponding to the –(OH) and -O functional group attached on the Ti$_3$C$_2$ surface[26,51]. The peak located at 530.1 eV can be assigned to the Ti-O bond which can be ascribed to the oxidation of the Ti$_3$C$_2$ MXene surface during the XPS measurement. In addition, although MXene oxidation is suppressed during the bisolvent synthesis compared to the aqueous-based method (see Supplementary Figs. 1, 2, and 3), a certain degree of undesired oxidation still took place during the solvothermal process. Moreover, two peaks at 532.3 eV and 532.8 eV can be attributed to the presence of Al$_2$O$_3$ related to the incomplete Al layer etching from the MAX phase and the adhesive water associated with the high hydrophilicity of the MXene surface, respectively[51]. In Fig. 4d, the peaks for Mo^{4+}(d3/2) and Mo^{4+}(d5/2) are located at 231.8 eV and 228. 6 eV, respectively, with an S^{2+} peak at 225.8 eV. It is noteworthy that a doublet (at 229.6 eV and 233.1 eV) for Mo^{5+} were observed, which is beneficial for the MoS$_2$ stability[52]. Besides that, Mo^{6+} shows a peak at 235.7 eV, suggesting partial oxidation of Mo, corresponding to the Raman observation in Fig. 3b. As for S 2p spectra, two doublets that emerged at 163.5/162.1 eV and 162.7/161.4 eV can be attributed to 2H-MoS$_2$ and 1T-MoS$_2$, respectively, reflecting the successful synthesis of mixed 1 T and 2H phase MoS$_2$, which is in good agreement with the previous TEM and Raman analysis in Supplementary Fig. 4c and Supplementary Fig. 6, respectively. Our calculation based on S 2p peak deconvolution suggested that the content of 1 T phase MoS$_2$ is around 66%, indicating a 1T-phase enriched structure in the dual-phase MoS$_2$. Figure 4f displays the Ti 2p spectra. The doublet located at 464.3 eV and 458.9 eV can be assigned to the Ti-O bond and resonate well with the observation in Fig. 4c. The two peaks at 465.1 eV and 459.4 eV represent the Ti-F bond, which is introduced during the Al layer etching process using HCl/LiF. The Ti-C bond-related peaks are observed at 461.2 eV and 456.6 eV, respectively, which are consistent with previous reports for MXene structures[26,50].

The HER performance and electrochemical characterizations

The electrochemical HER activity exploration of as-synthesized MoS$_2$-based electrocatalysts was conducted in 0.5 M H$_2$SO$_4$ using a standard three-electrode configuration with the built-in IR compensation function. Figure 5a, b display the LSV curves and corresponding Tafel plots of as-prepared samples. The pristine CNT and Ti$_3$C$_2$ MXene show nearly inert HER activity with a horizontal LSV curve pattern, indicating a limited HER activity of
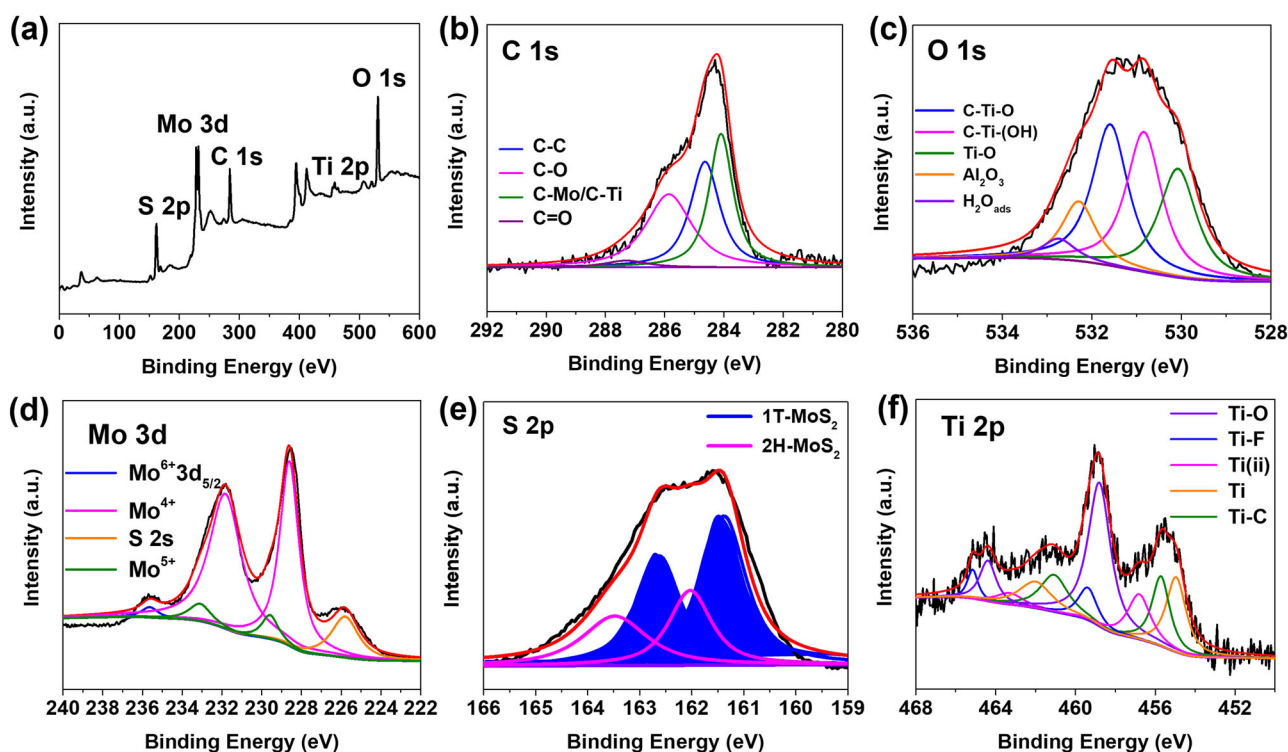
Fig. 4 The XPS characterization of the MTC composite. a The complete XPS survey spectra of MTC100. Deconvoluted XPS spectra showing the binding energy of (**b**) carbon, **c** Oxygen, **d** Molybdenum, **e** Sulfur, **f** Titanium, respectively.
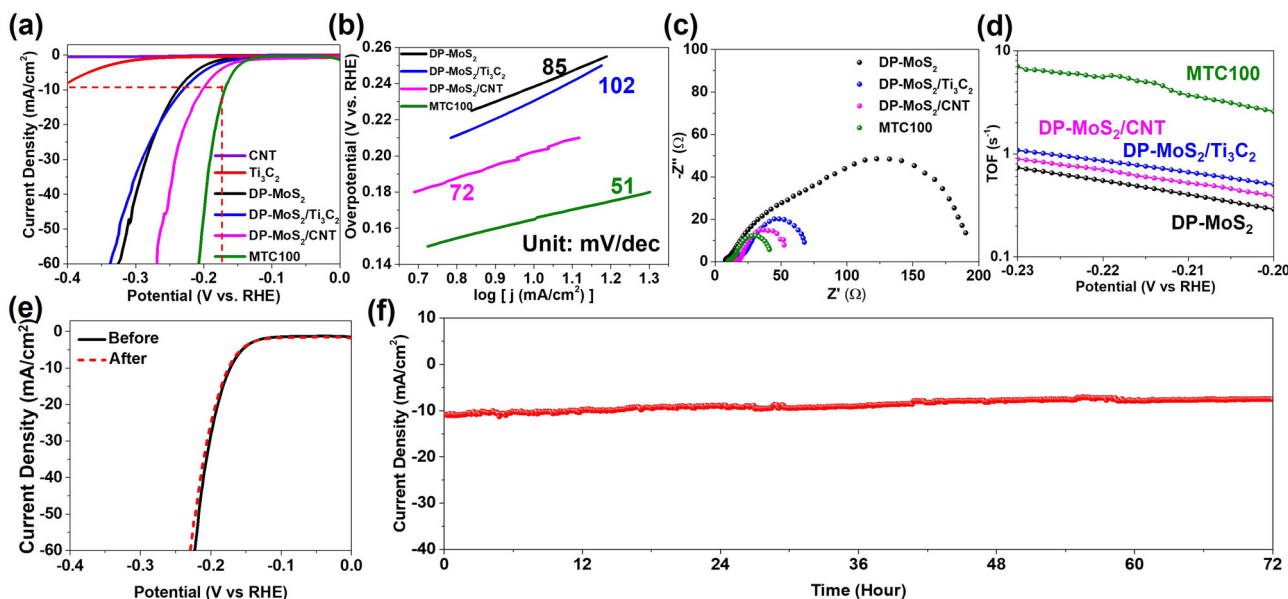

Fig. 5 The electrochemical performance evaluation. a Polarization curves measured at a scan rate of 5 mV/s. **b** Tafel plots for selected samples. **c** The Nyquist plot of different samples. **d** The turnover frequency versus potential plot. **e** The polarization curves of MTC100 before and after 1000 cycles of CV scans. **f** The time-dependent stability plot.

CNT and Ti_3C_2. The DP-MoS_2 exhibits a much lower overpotential of 238 mV at a current density of 10 mA/cm^2 (η_{10}) and a low Tafel slope of 85 mV/dec due to the higher intrinsic catalytic capability of DP-MoS_2 compared to the aqueous-synthesized 2H-MoS_2 (Supplementary Fig. 7a, b). The enhanced HER performance can be ascribed to the significantly reduced charge transfer resistance (R_{ct}) associated with the high conductivity of the metallic 1 T phase (Supplementary Fig. 7c). In the case of binary composites, the DP-MoS_2/CNT enabled a better HER performance compared

with DP-MoS_2/Ti_3C_2, evidenced by a lower overpotential and a smaller Tafel slope (202 mV, 72 mV/dec and 230 mV, 102 mV/dec for CNT and Ti_3C_2 composites, respectively), which can be attributed to the smaller R_{ct} of DP-MoS_2/CNT (see Fig. 5c) because of the higher conductivity of CNT with respect to Ti_3C_2[21,53] and the crosslink function of CNTs bridging different 2D MoS_2 islands (see Fig. 2e) for a universal conductive network formation. Among all the structures, MTC100 exhibits the lowest η_{10} of 169 mV and the smallest Tafel slope of 51 mV/dec, which can be associated with

the smallest R_{ct} (see Fig. 5c) originated from the highest overall electrical conductivity via constructing a 1T-phase enriched MoS_2-based 1D/2D hybrid network. It is worth mentioning that the MTC100 shows excellent performance reproducibility. The over-potentials were found to be 169 ± 5 mV for four different catalyst inks fabricated using the same batch of MTC100 sample that has been stored for around 1 year.

The CV was carried out to determine the double-layer capacitance (C_{dl}) and to calculate the electrochemical surface area (ECSA), as shown in Supplementary Fig. 8. The measured C_{dl} for Ti_3C_2 MXene, DP-MoS_2, DP-MoS_2/Ti_3C_2, DP-MoS_2/CNT and MTC100 is 36, 6, 34, 27 and 44 mF/cm^2, and the corresponding ECSA are calculated to be 882, 144, 838, 676, and 1099 cm^2, respectively (see Supplementary Table 1). The BET specific surface area was also tested by N_2 adsorption/desorption isotherm, as shown in Supplementary Fig. 9a. The result shows that MTC100 contains the largest surface area of 32 m^2/g, which is larger compared to the other binary composites (DP-MoS_2, DP-MoS_2/Ti_3C_2, and DP-MoS_2/CNT exhibit the BET area of 21, 18, and 28 m^2/g, respectively). As can be seen in Supplementary Fig. 9b, the pore size lies in the range of 10~50 nm, suggesting a mesopore-enriched structure of the DP-MoS_2 hybrids[54]. The enriched porosity feature can be attributed to the gas evolution during the solvothermal synthesis of the flower-shaped MoS_2-based hybrid structure and the integrated stacking nature of the 2D MoS_2/MXene layered hybrids[17,32,55–57]. The turnover frequency (TOF) is another vital parameter to evaluate the activity of an HER electrocatalyst which characterizes the intrinsic activity of an electrocatalyst at a single active site. By combining the TOF with overpotential, it can provide a more comprehensive and in-depth view of the kinetics and a robust basis of catalytic benchmarking[58]. The TOF values of the above-mentioned samples were calculated based on the CV measurement in a pH-neutral phosphate buffer solution and were plotted in Fig. 5d in the range of 0.2~0.23 V. It is worth mentioning that the TOF of DP-MoS_2/CNT is lower than that of DP-MoS_2/Ti_3C_2 despite the smaller R_{ct} as shown in Fig. 5c, which is due to CNTs exhibit inherently low catalytic activity (see Fig. 5a) and limited contribution to the interlayer spacing expansion and surface area enlargement (see Fig. 3a, Supplementary Fig. 8, and Supplementary Fig. 9). Among all the samples, DP-MTC100 exhibits a superior TOF corresponding to the observed higher catalytic activity compared to the other DP-MoS_2-based binary composites. The origin of the outstanding HER performance for the ternary composite lies in threefold: (i) the enlarged surface area due to the 2D/2D MoS_2/Ti_3C_2 integration and ion intercalation which promotes the contact between electrolyte and catalyst, leading to an increased hydrogen ion adsorption; (ii) the vertically grown MoS_2 flakes on the Ti_3C_2 template ensures the maximum exposure of MoS_2 edge planes which is beneficial to increase the total number of active sites; (iii) the synergistically enhanced conductivity due to the existence of 1T-phase enriched metallic MoS_2, the conductive backbone of Ti_3C_2 along with the crosslink function of CNTs, minimizing the charge transfer resistance at the electrode/electrolyte interface.

To investigate the cycling stability, the CV measurements between −0.2 and 0.3 V were performed and the polarization curves before and after cycling are shown in Fig. 5e. A negligible shift of the polarization curve after 1000 CV cycles was observed, suggesting a long lifetime of DP-MTC100 in the acidic media. The superior ternary catalyst stability is benefited from the integration of MoS_2 with Ti_3C_2 which not only partially suppressed the Ti_3C_2 oxidation but also prevent the 2D layer restacking. In addition, it is known that the 1 T phase MoS_2 is metastable and easily converted to the stable 2H phase, leading to the performance degradation of 1 T metallic MoS_2-based devices[13,59]. In our case, the NH_4^+ intercalation can serve as the electron donor to stabilize the 1 T phase and therefore reduce the tendency of phase conversion[60]. The ultralong time stability of DP-MTC100 is again confirmed by

the time-dependent stability measurement as shown in Fig. 5f. The current density was measured at an overpotential of 169 mV and was stabilized at near 10 mA/cm^2 for 72 h. The stability retention was extracted to be 95% at the 30 h and 77% at the 72 h, respectively. Nevertheless, activity loss can still be observed since the slow phase conversion of 1 T to 2H and the mild oxidation of the structure still take place to a certain degree inevitably in a long run.

HER performance evaluation of MTC hybrids with different CNT ratios

To optimize the HER activity, we synthesized four different ternary DP-MTC samples with different weights of CNTs (50, 70, 100, and 200 mg). As shown in Fig. 6, the MTC100 outperforms the other ternary hybrids, evidenced by the smallest overpotential (169 mV) and a small Tafel slope (51 mV/dec). It is noteworthy that MTC200 displays an even smaller Tafel slope (49 mV/dec) and the lowest R_{ct} value among the ternary composites (see Fig. 6b, c), which can be ascribed to the higher ratio of CNTs that further enhanced the network conductivity and therefore charge transfer efficiency during the reaction. However, the TOF of MTC200 is one of the smallest among different CNT composites along with a large overpotential (216 mV), as shown in Fig. 6a, d. It is well known that the number of active sites and the electrical conductivity are two vital factors for determining the HER activity of the electrocatalyst. In our case, the conductivity of the ternary composites improved significantly by adding more CNTs. However, the intrinsically low catalytic activity of CNT (see Fig. 5a) and its limited contribution to the surface area enlargement impacts the HER activity adversely. In addition, the relatively high CNT ratio will decrease the content of DP-MoS_2, leading to a decreased total number of active sites and therefore the catalytic activity correspondingly. Overall, the MTC100 provides a well-balanced relationship between the electrical conductivity and the number of active sites and therefore delivered the best catalytic performance for HER.

DISCUSSION

In summary, we successfully synthesized a ternary, dual-phase MoS_2/Ti_3C_2/CNT structure by a one-step solvothermal technique, and investigated its HER activity. Such a ternary hybrid composite exhibited superior structure advantages compared to the other binary counterparts in terms of enlarged surface area, increased number of active sites, and a well-constructed 1D/2D hybrid conductive network. The 2D domains of metallic phase-enriched MoS_2 and the Ti_3C_2 conductive backbone were bridged by the 1D CNTs and therefore synergistically boosted the overall network conductivity. The composition-performance relationship interrogation revealed that the amount of CNTs in the composite is a determining factor for HER performance. The long-term catalytic stability was also achieved by the integration of MoS_2 with Ti_3C_2 in bisolvent media which effectively prevented the 2D layer restacking and partially suppressed the Ti_3C_2 oxidation. Our work demonstrated an effective strategy for low-dimensional material structure-property engineering with the aim of optimizing the device performance and shedding light on the development of the next-generation PGM-free HER electrocatalysts.

METHODS

Materials

Anhydrous ethanol, lithium fluoride (LiF), hydrochloric acid (HCl), ammonium molybdate, thiourea and N, N-dimethylformamide (DMF) were purchased from Fisher Scientific, USA. Ti_3AlC_2 was purchased from Beijing Forsman Scientific Co. Ltd., China. Multiwalled carbon nanotubes (CNT) were purchased from XFNANO, China. All chemicals were used as received without any further purification.
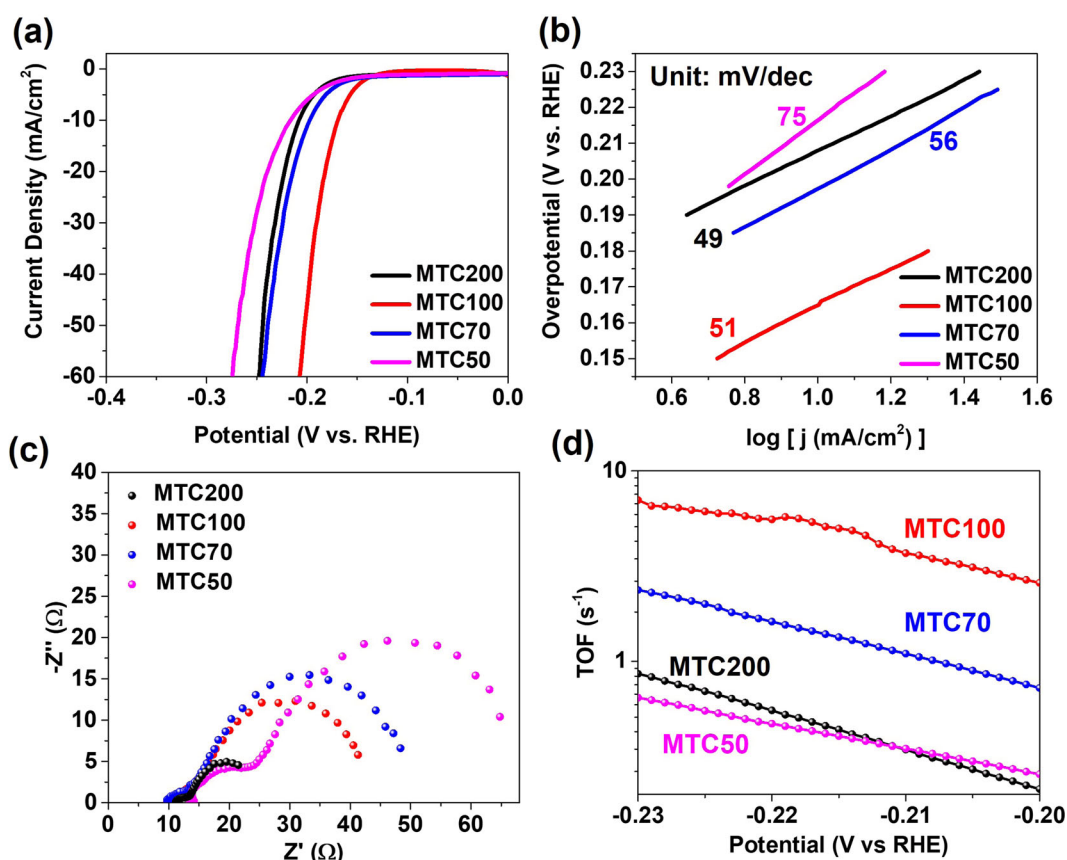
Fig. 6 The electrochemical results of MTC hybrids with different CNT ratios. a The polarization curves, **b** The Tafel plots, **c** The Nyquist plots, **d** The turnover frequency versus potential plots of MTC ternary composites with different CNT amounts.

Preparation of Ti$_3$C$_2$ MXene

The Ti$_3$C$_2$ was prepared by the in situ HF etching method[31]. Specifically, 2 g LiF powder was slowly added into 40 ml HCl (9 M) solution and stirred for 30 min until the LiF was fully dissolved. 2 g Ti$_3$AlC$_2$ was slowly added into the LiF/HCl mixture which was placed in an ice bath subsequently. The solution was kept at 40 °C for 48 h with continuous stirring. After the reaction, the black powder was collected by centrifugation and washed with DI water until the supernatant reached a pH value of 6. The powder was dried under vacuum at 60 °C for 12 h.

Synthesis of the dual-phase MoS$_2$/Ti$_3$C$_2$/CNT (DP-MTC) ternary composite

1 g of as-prepared Ti$_3$C$_2$ powder and 0.1 g CNT were added into 60 mL DI/DMF (volume ratio 1:1) bisolvent, followed by ultrasonication to form a homogenous suspension. 1.928 g ammonium molybdate and 3.645 g of thiourea were slowly added into the suspension and stirred until the precursors were well mixed. The suspension was then transferred into a 100 mL Teflon-lined autoclave and kept at 195 °C for 22 h. After naturally cooling down to room temperature, the product was collected by centrifugation and washed with DI/ethanol, followed by vacuum drying at 60 °C for overnight. The as-prepared sample was denoted as DP-MTC100 where the number indicated the weight of CNT (100 mg). Different binary composites (MoS$_2$/Ti$_3$C$_2$, MoS$_2$/CNT) and MTC hybrid structures with different MXene to CNT ratios were also synthesized as control samples. To evaluate the influence of bisolvent impact in the synthesis, the MoS$_2$ powder and MoS$_2$/Ti$_3$C$_2$ composite (denoted as 2H-MoS$_2$ and 2H-MoS$_2$/Ti$_3$C$_2$, respectively) was also synthesized with the same precursor concentration in DI water as a reference sample.

Characterization

X-ray diffraction (XRD) was performed using a Rigaku Ultima IV with Cu Kα radiation (wavelength = 1.541 nm). Raman spectra were collected using Renishaw InVia with an excitation laser wavelength of 514 nm. The morphologies of all products were investigated by field-emission scanning

electron microscope (FE-SEM, Carl Zeiss AURIGA CrossBeam with Oxford energy dispersive x-ray spectra (EDS) system). The transmission electron microscopy (TEM) was conducted using the JEM ARM 200 F system. X-ray photoelectron spectroscopy (XPS) was performed using a monochromatic Al Kα source (hv = 1486.6 eV) (ESCALAB 250, Thermo Scientific). The Brunauer-Emmett-Teller (BET) measurements were conducted on a Micromeritics Tri-Star II system by nitrogen (N$_2$) adsorption-desorption isotherm at 77 K.

Electrochemical measurements

The ink for the HER test was prepared by dissolving 10 mg of as-prepared powder in a mixture of 500 μL of ethanol, 500 μL of DI water, and 15 μL of Nafion D-521 solution. The electrochemical characterization was performed using CHI760E electrochemical workstation (CH Instrument) in a standard three-electrode system which consists of a silver/silver chloride (Ag/AgCl in 1 M KCl), a platinum (Pt) wire, and an ink-coated glassy carbon rotating ring disc electrode as reference, counter and working electrodes, respectively. The loading amount of the sample is 0.285 mg/cm^2 and the samples were cycled 20 times before any data recording. Nitrogen gas saturated 0.5 M H$_2$SO$_4$ was employed as electrolyte. All the measured potentials were converted to the potential vs. E$_{RHE}$ based on the equation: E$_{RHE}$ = E$_{Ag/AgCl}$ + 0.059 pH + 0.222. The linear sweep voltammetry (LSV) was carried out at a scan rate of 5 mV/s and the built-in IR compensation was executed prior to LSV tests. The electrochemical impedance spectroscopy (EIS, Biologic VMP3) was conducted from 0.1 Hz to 1 MHz with an amplitude of 5 mV at an overpotential of 250 mV vs. RHE. The electrochemical surface area was tested by cyclic voltammetry (CV) in the potential range of 0.05–0.15 V vs. RHE with different scan rates (20, 40, 50, 60, 80, and 100 mV/s). The double-layer capacitance (C$_{dl}$) was assessed from the slope of the linear regression between the current density differences (ΔJ/2 = (J$_{anode}$-J$_{cathode}$)/2 at an overpotential of 0.1 V vs. RHE) versus the scan rates. The accessible surface area of as-synthesized samples could be approximated from the electrochemical active surface area (ECSA). The ECSA was determined by ECSA = C$_{dl}$/C$_s$, where C$_s$ stands for the specific capacitance of standard electrode materials on a unit

surface area. Here, based on the literature reported Cs values for carbon electrode materials, 0.04 mF/cm^2 was used for ECSA calculations[61]. CV was performed between −0.3 V and 0.2 V vs. RHE to check the cycle stability.

DATA AVAILABILITY

All data generated or analysed during this study are included in this published article (and its supplementary information files).

REFERENCES

1. Greeley, J., Jaramillo, T. F., Bonde, J., Chorkendorff, I. & Nørskov, J. K. Computational high-throughput screehrning of electrocatalytic materials for hydrogen evolution. *Nat. Mater.* **5**, 909–913 (2006).
2. Morales-Guio, C. G., Stern, L. A. & Hu, X. Nanostructured hydrotreating catalysts for electrochemical hydrogen evolution. *Chem. Soc. Rev.* **43**, 6555–6569 (2014).
3. Voiry, D., Yang, J. & Chhowalla, M. Recent strategies for improving the catalytic activity of 2D TMD nanosheets toward the hydrogen evolution reaction. *Adv. Mater.* **28**, 6197–6206 (2016).
4. Hinnemann, B. et al. Biomimetic hydrogen evolution: MoS$_2$ nanoparticles as catalyst for hydrogen evolution. *J. Am. Chem. Soc.* **127**, 5308–5309 (2005).
5. Jiao, Y., Zheng, Y., Jaroniec, M. & Qiao, S. Z. Design of electrocatalysts for oxygen- and hydrogen-involving energy conversion reactions. *Chem. Soc. Rev.* **44**, 2060–2086 (2015).
6. Zou, X. & Zhang, Y. Noble metal-free hydrogen evolution catalysts for water splitting. *Chem. Soc. Rev.* **44**, 5148–5180 (2015).
7. She, Z. W. et al. Combining theory and experiment in electrocatalysis: Insights into materials design. *Science* **355**, eaad4998 (2017).
8. Zheng, Y., Jiao, Y., Jaroniec, M. & Qiao, S. Z. Advancing the electrochemistry of the hydrogen- Evolution reaction through combining experiment. *Angew. Chem. Int. Edi.* **54**, 52–65 (2015).
9. Guo, Y. et al. Nanoarchitectonics for transition-metal-sulfide-based electrocatalysts for water splitting. *Adv. Mater.* **31**, 1807134 (2019).
10. Xia, X., Wang, L., Sui, N., Colvin, V. L. & Yu, W. W. Recent progress in transition metal selenide electrocatalysts for water splitting. *Nanoscale* **12**, 12249–12262 (2020).
11. Gao, Q., Zhang, W., Shi, Z., Yang, L. & Tang, Y. Structural design and electronic modulation of transition-metal-carbide electrocatalysts toward efficient hydrogen evolution. *Adv. Mater.* **31**, 1802880 (2019).
12. Li, H. et al. Activating and optimizing MoS$_2$ basal planes for hydrogen evolution through the formation of strained sulphur vacancies. *Nat. Mater.* **15**, 48–53 (2016).
13. Acerce, M., Voiry, D. & Chhowalla, M. Metallic 1T phase MoS$_2$ nanosheets as supercapacitor electrode materials. *Nat. Nanotechnol.* **10**, 313–318 (2015).
14. Lin, Y. C., Dumcenco, D. O., Huang, Y. S. & Suenaga, K. Atomic mechanism of the semiconducting-to-metallic phase transition in single-layered MoS2. *Nat. Nanotechnol.* **9**, 391–396 (2014).
15. Yin, Y. et al. Contributions of phase, sulfur vacancies, and edges to the hydrogen evolution reaction catalytic activity of porous molybdenum disulfide nanosheets. *J. Am. Chem. Soc.* **138**, 7965–7972 (2016).
16. Shang, B. et al. Lattice -mismatch-induced ultrastable 1T-Phase MoS$_2$-Pd/Au for plasmon-enhanced hydrogen evolution. *Nano Lett.* **19**, 2758–2764 (2019).
17. Strachan, J., Masters, A. F. & Maschmeyer, T. Critical review: Hydrothermal synthesis of 1T-MoS$_2$-an important route to a promising material. *J. Mater. Chem. A* **9**, 9451–9461 (2021).
18. Shi, S., Sun, Z. & Hu, Y. H. Synthesis, stabilization and applications of 2-dimensional 1T metallic MoS$_2$. *J. Mater. Chem. A* **6**, 23932–23977 (2018).
19. Naguib, M., Mochalin, V. N., Barsoum, M. W. & Gogotsi, Y. 25th anniversary article: MXenes: A new family of two-dimensional materials. *Adv. Mater.* **26**, 992–1005 (2014).
20. Naguib, M. et al. Two-dimensional transition metal carbides. *ACS Nano.* **6**, 1322–1331 (2012).
21. Anasori, B., Lukatskaya, M. R. & Gogotsi, Y. 2D metal carbides and nitrides (MXenes) for energy storage. *Nat. Rev. Mater.* **2**, 16098 (2017).
22. Ghidiu, M., Lukatskaya, M. R., Zhao, M. Q., Gogotsi, Y. & Barsoum, M. W. Conductive two-dimensional titanium carbide "clay" with high volumetric capacitance. *Nature* **516**, 78–81 (2014).
23. Lukatskaya, M. R. et al. Cation intercalation and high volumetric capacitance of two-dimensional titanium carbide. *Science* **341**, 1500–1502 (2013).
24. Lukatskaya, M. R. et al. Ultra-high-rate pseudocapacitive energy storage in two-dimensional transition metal carbides. *Nat. Energy* **6**, 17105 (2017).
25. Yan, J. et al. Flexible MXene/Graphene films for ultrafast supercapacitors with outstanding volumetric capacitance. *Adv. Funct. Mater.* **27**, 1701264 (2017).
26. Attanayake, N. H. et al. Vertically aligned MoS$_2$ on Ti$_3$C$_2$ (MXene) as an improved HER catalyst. *J. Mater. Chem. A* **6**, 16882–16889 (2018).
27. Ran, J. et al. Ti$_3$C$_2$ MXene co-catalyst on metal sulfide photo-absorbers for enhanced visible-light photocatalytic hydrogen production. *Nat. Commun.* **8**, 13907 (2017).
28. Gao, G., O'Mullane, A. P. & Du, A. 2D MXenes: A new family of promising catalysts for the hydrogen evolution reaction. *ACS Catal.* **7**, 494–500 (2017).
29. Chen, C. et al. MoS$_2$-on-MXene Heterostructures as highly reversible anode materials for lithium-ion batteries. *Angew. Chem. Int. Ed.* **130**, 1864–1868 (2018).
30. Wu, Y. et al. MoS$_2$-nanosheet-decorated 2D titanium carbide (MXene) as high-performance anodes for sodium-ion batteries. *Chem. Electro. Chem.* **4**, 1560–1565 (2017).
31. Alhabeb, M. et al. Guidelines for synthesis and processing of two-dimensional Titanium Carbide (Ti$_3$C$_2$T$_x$ MXene). *Chem. Mater.* **29**, 7633–7644 (2017).
32. Ji, L. et al. One-pot synthesis of porous 1T-phase MoS$_2$ integrated with single-atom Cu doping for enhancing electrocatalytic hydrogen evolution reaction. *Appl. Catal. B* **251**, 87–93 (2019).
33. Zhang, Y., Kuwahara, Y., Mori, K., Louis, C. & Yamashita, H. Hybrid phase 1T/2H-MoS$_2$ with controllable 1T concentration and its promoted hydrogen evolution reaction. *Nanoscale* **12**, 11908–11915 (2020).
34. Xiang, T. et al. Vertical 1T-MoS$_2$ nanosheets with expanded interlayer spacing edged on a graphene frame for high rate lithium-ion batteries. *Nanoscale* **9**, 6975–6983 (2017).
35. Cao, M. et al. Room temperature oxidation of Ti$_3$C$_2$ MXene for supercapacitor electrodes. *J. Electrochem. Soc.* **164**, A3933–A3942 (2017).
36. Slot, T. K. et al. Surface oxidation of Ti$_3$C$_2$T$_x$ enhances the catalytic activity of supported platinum nanoparticles in ammonia borane hydrolysis. *2D Mater.* **8**, 015001 (2020).
37. Wu, M. et al. Metallic 1T MoS$_2$ nanosheet arrays vertically grown on activated carbon fiber cloth for enhanced Li-ion storage performance. *J. Mater. Chem. A* **5**, 14061–14069 (2017).
38. Simon, P. Two-dimensional MXene with controlled interlayer spacing for electrochemical energy storage. *ACS Nano.* **11**, 2393–2396 (2017).
39. Ling, Z. et al. Flexible and conductive MXene films and nanocomposites with high capacitance. *Proc. Natl Acad. Sci. USA.* **111**, 16676–16681 (2014).
40. Wang, F. et al. ZnO nanoparticle-decorated two-dimensional titanium carbide with enhanced supercapacitive performance. *RSC Adv.* **6**, 88934–88942 (2016).
41. Tariq, A., Ali, S. I., Akinwande, D. & Rizwan, S. Efficient visible-light photocatalysis of 2D-MXene nanohybrids with Gd^{3+}- and Sn^{4+}-codoped bismuth ferrite. *ACS Omega* **3**, 13828–13836 (2018).
42. Lei, Z., Zhan, J., Tang, L., Zhang, Y. & Wang, Y. Recent development of metallic (1T) phase of molybdenum disulfide for energy conversion and storage. *Adv. Energy Mater.* **8**, 1703482 (2018).
43. Li, X. et al. Ti$_3$C$_2$ MXenes modified with: In situ grown carbon nanotubes for enhanced electromagnetic wave absorption properties. *J. Mater. Chem. C.* **5**, 4068–4074 (2017).
44. Dong, Y. et al. Ti$_3$C$_2$ MXene-derived Sodium/Potassium Titanate nanoribbons for high-performance sodium/potassium ion batteries with enhanced capacities. *ACS Nano.* **11**, 4792–4800 (2017).
45. Li, H. et al. From bulk to monolayer MoS$_2$: Evolution of Raman scattering. *Adv. Funct. Mater.* **22**, 1385–1390 (2012).
46. Chung, D. Y. et al. Edge-exposed MoS$_2$ nano-assembled structures as efficient electrocatalysts for hydrogen evolution reaction. *Nanoscale* **6**, 2131–2136 (2014).
47. Wang, D. et al. Phase engineering of a multiphasic 1T/2H MoS$_2$ catalyst for highly efficient hydrogen evolution. *J. Mater. Chem. A* **5**, 2681–2688 (2017).
48. Chang, J. et al. Asymmetric supercapacitors based on graphene/MnO$_2$ nanospheres and graphene/MoO$_3$ nanosheets with high energy density. *Adv. Funct. Mater.* **23**, 5074–5083 (2013).
49. Dresselhaus, M. S., Dresselhaus, G., Saito, R. & Jorio, A. Raman spectroscopy of carbon nanotubes. *Phys. Rep.* **409**, 47–99 (2005).
50. Liu, J. et al. Hierarchical "nanoroll" like MoS$_2$/Ti$_3$C$_2$T$_x$ hybrid with high electrocatalytic hydrogen evolution activity. *Appl. Catal. B* **241**, 89–94 (2019).
51. Shen, C. et al. MoS$_2$-decorated Ti$_3$C$_2$ MXene nanosheet as anode material in lithium-ion batteries. *J. Electrochem. Soc.* **164**, A2654–A2659 (2017).
52. Li, J. et al. Graphene-MoS$_2$ vertically anchored on an MXene-derived accordion-like TiO$_2$/C skeleton: An ultrastable HER catalyst. *J. Mater. Chem. A* **8**, 14223–14233 (2020).
53. Miao, M. Electrical conductivity of pure carbon nanotube yarns. *Carbon* **49**, 3755–3761 (2011).
54. Cook, J. B. et al. Mesoporous MoS$_2$ as transition metal dichalcogenide exhibiting pseudocapacitive Li and Na-ion charge storage. *Adv. Energy Mater.* **6**, 1501937 (2016).
55. Wang, F. et al. Hydrothermal synthesis of flower-like molybdenum disulfide microspheres and their application in electrochemical supercapacitors. *RSC Adv.* **8**, 38945–38954 (2018).
56. Zhang, X. et al. Hydrothermal synthesis and characterization of 3D flower-like MoS$_2$ microspheres. *Mater. Lett.* **148**, 67–70 (2015).

57. Kadam, S. R. et al. Porous MoS₂ framework and its functionality for electrochemical hydrogen evolution reaction and lithium ion batteries. *ACS Appl. Energy Mater.* **2**, 5900–5908 (2019).

58. Costentin, C. & Savéant, J. M. Towards an intelligent design of molecular electrocatalysts. *Nat. Rev. Chem.* **1**, 0087 (2017).

59. Yu, Y. et al. High phase-purity 1T′-MoS₂- and 1T′-MoSe₂-layered crystals. *Nat. Chem.* **10**, 638–643 (2018).

60. Liu, Q. et al. Gram-scale aqueous synthesis of stable few-layered 1T-MoS₂: Applications for visible-light-driven photocatalytic hydrogen evolution. *Small* **11**, 5556–5564 (2015).

61. Deng, H. et al. Laser induced MoS₂/carbon hybrids for hydrogen evolution reaction catalysts. *J. Mater. Chem. A* **4**, 6824–6830 (2016).

AUTHOR CONTRIBUTIONS

S.C.W. Y.F., M.M.L., and H.Y.Y. conducted the material synthesis and characterization. S.W.P. and Y.H.L. performed the TEM characterization. H.M.L. and F.Y. guided the project and wrote the paper. All authors reviewed the paper.

COMPETING INTERESTS

The authors declare no competing interests.

ADDITIONAL INFORMATION

Supplementary information The online version contains supplementary material available at https://doi.org/10.1038/s41699-022-00300-0.

Correspondence and requests for materials should be addressed to Huamin Li or Fei Yao.

Reprints and permission information is available at http://www.nature.com/reprints

Publisher's note Springer Nature remains neutral with regard to jurisdictional claims in published maps and institutional affiliations.